



Performance of Magnéli phase Ti_4O_7 and Ti^{3+} self-doped TiO_2 as oxygen vacancy-rich titanium oxide anodes: Comparison in terms of treatment efficiency, anodic degradative pathways, and long-term stability

Minjeong Kim^a, Jaemin Choi^a, Woonghee Lee^b, Yong-Yoon Ahn^c, Hangil Lee^d, Kangwoo Cho^b, Jaesang Lee^{a,*}

^a Civil, Environmental, and Architectural Engineering, Korea University, Seoul 02841, Republic of Korea

^b Environmental Science and Engineering, Pohang University of Science and Technology (POSTECH), Pohang 37673, Republic of Korea

^c Korea Polar Research Institute (KOPRI), Incheon 21990, Republic of Korea

^d Chemistry, Sookmyung Women's University, Seoul 04310, Republic of Korea

ARTICLE INFO

Keywords:

Anodic oxidation
Magnéli phases
 Ti^{3+} self-doped TiO_2
Hydroxyl radical
Long-term stability

ABSTRACT

This study compared hydrogen annealing and cathodic polarization (producing Magnéli phases and Ti^{3+} self-doped TiO_2 , respectively) as strategies to fabricate electrically conducting titanium oxides through oxygen non-stoichiometry creation for anodic water treatment. Electrochemical characterization techniques suggested that Ti_4O_7 best-suited for redox electrocatalysis among the Magnéli phases exhibited higher electrical conductivity than the self-doped TiO_2 . This aligned with the superiority of Ti_4O_7 over the self-doped TiO_2 in chlorine evolution and anodic organic oxidation. Hydroxyl radical primarily contributed to anodic oxidation by two conductive titanium oxides at sulfate-based electrolyte, based on the retarding effects of radical scavengers, multi-activity assessment, electron paramagnetic resonance spectral features, and product distribution. Repetitive batch experiments and long-term tests in continuous operation mode demonstrated that self-doped TiO_2 underwent more drastic performance reduction than Ti_4O_7 . This accorded with the self-doped TiO_2 being more vulnerable to activity loss, chemical alteration, and structural damage during prolonged application.

1. Introduction

Electrochemical water treatment has been recognized as an appealing technical option for the oxidative degradation of aquatic organic pollutants owing to (i) high-yield production of multiple radical and non-radical oxidants via the anodic oxidation of water/ OH^- and electrolytes, (ii) minimal need for external chemical supply, (iii) ease of process operation and maintenance, and (iv) integration with renewable energy production/storage systems [1–3]. Together with reaction parameters of electrolyte type, pH, and applied voltage, the choice of anode material is a key to the overall performance of electrochemical oxidation processes for water treatment and disinfection [2,4]. Anodes with high oxygen evolution reaction (OER) overpotentials, such as boron-doped diamond (BDD) and PbO_2 , classified as being non-active according to Comninellis' model [4], were demonstrated to oxidatively decompose a broad spectrum of organics primarily due to their capability to generate hydroxyl radicals ($\cdot\text{OH}$) [5,6]. On the other hand,

low OER overpotential anodes, such as IrO_2 and RuO_2 , exhibit substrate-sensitive treatment efficiency; radical intermediates resulting from water electrolysis strongly interact with the active anodes, transforming into the chemisorbed oxygen species with selective reactivity [7,8]. Hence, BDD has been typically adopted for the anodic oxidation and mineralization of highly persistent wastewaters whereas dimensionally stable anode (DSA) comprising IrO_2 , RuO_2 , or their mixtures is reputed to be best suited for the chlorine evolution reaction (CER).

As an alternative to the conventional anodes having drawbacks associated with high manufacturing cost, the use of noble metals, or secondary contamination with released metal components, select metal-oxide semiconductors possessing oxygen-deficient compositions or local non-stoichiometry of oxygen have been explored for the anodic oxidation of organic pollutants [9–13]. Implantation of oxygen vacancies (OVs) improves the metallic character of metal oxides by modifying the band-gap structures and increasing the population of electrons (free or loosely bound to the vacancies), thus rendering some semiconductors,

* Corresponding author.

E-mail address: lee39@korea.ac.kr (J. Lee).

<https://doi.org/10.1016/j.apcatb.2023.122993>

Received 3 March 2023; Received in revised form 5 June 2023; Accepted 11 June 2023

Available online 12 June 2023

0926-3373/© 2023 Elsevier B.V. All rights reserved.

such as TiO_2 and WO_3 , technically adequate for application as anode materials [14–16]. The strategies to fabricate electrically conductive OV-rich metal oxides from the stoichiometric counterparts without heteroatom doping include heat treatment in a reducing atmosphere, reduction using chemical agents (e.g., Li and NaBH_4), and cathodic modification [14]. For example, high-temperature calcination in an inert gas or hydrogen atmosphere caused the substantial loss of oxygen atoms from the oxide lattice and altered the oxygen-to-metal ratios in the entire crystalline matrices, producing stable metal suboxides (e.g., W_5O_{14} and Ti_3O_5) [16,17]. Hydrogen annealing [18] and (electro)chemical reduction [13,19,20] promoted the activity of metal oxides for (photo)electrocatalysis by creating the pairs of OV-metal interstitial as surface or subsurface species in metal oxides (i.e., self-doping).

Titanium oxides, which have been successfully demonstrated to enable oxidation-based electrochemical water treatment and disinfection [11–13,20,21], take two primary forms: Magnéli phase titanium suboxides with the general formula $\text{Ti}_n\text{O}_{2n-1}$ (n as an integer varies in the range of 3–10 [16]) and Ti^{3+} self-doped TiO_2 . Cyclic voltammetric studies [22,23] confirmed that the Ti-based anodes possessed wide potential windows for water electrolysis and high OER overpotentials (exceeding ~ 2.5 V vs. Ag/AgCl) as a prerequisite for anodic $\bullet\text{OH}$ production. Magnéli phases whose structures conceptually comprise a stack of TiO_2 layers with every n^{th} layer having oxygen deficiency are identified as electrically conductive and chemically robust titanium oxides [16,24,25]. In particular, Ti_4O_7 with the highest electrical conductivity among Magnéli phases (comparable to that of graphite [26]) is technically adequate to yield $\bullet\text{OH}$ during electrolysis [23], being widely used as the non-active anode for the treatment of diverse organic contaminants, including amoxicillin [11], paracetamol [27], and tetracycline [28]. Facile fabrication under ambient conditions and good controllability of doping levels have shed new light on cathodization as a competitive approach to introduce Ti^{3+} and OVs in TiO_2 [13,20]. Performance tests implied that Ti^{3+} self-doped TiO_2 (called “Blue TiO_2 ”, due to the blue coloration associated with irreversible electrochromism [29]) could serve as a leading alternative to the benchmark anodes such as BDD and DSA based on the excellence in electrocatalytic organic degradation and radical/non-radical oxidant yield [29,30]. The previous studies have often highlighted the relative superiority of the non-stoichiometric titanium oxides over the existing anodes [11,13,20,23,28–30]. However, the unbiased comparative assessment with a special focus on the electrochemical characteristics, treatment performance, and degradative pathway(s) of Magnéli phases and Ti^{3+} self-doped TiO_2 as the representative conductive titanium oxides, imperative for water professionals to make an informed choice of anode materials, has yet to be systematically made. Further, the relative position of Ti^{3+} self-doped TiO_2 , suggested to be stable based on the minor variation in Ti^{3+} content and no significant decline in treatment performance during the repeated photocatalytic and (photo)electrocatalytic organic degradation [31–33], needs to be evaluated against Magnéli phases in terms of applicability for prolonged anodic oxidation.

To address a knowledge gap in the possible differences in electrocatalytic behaviors that arise from the selection of different approaches to create OVs, in this study, we revisited the potentials of two conductive titanium oxides prepared via hydrogen annealing (Magnéli phase Ti_4O_7) and cathodic polarization (Blue TiO_2 (B- TiO_2)) of TiO_2 nanotube arrays (NTAs) for anodic water treatment. The electrochemical characterizations of Magnéli phases (prepared at different annealing temperatures) and B- TiO_2 were performed by cyclic voltammetry (CV), electrochemical impedance spectroscopy (EIS), and scanning electrochemical microscopy (SECM). Their capability for anodic oxidation was comparatively evaluated based on the efficacies of 4-chlorophenol degradation, oxidative conversion of methanol into formaldehyde, and hypochlorous acid production. The major oxidants generated during electrolysis using Ti_4O_7 and B- TiO_2 were identified through (i) the effects of radical scavengers on treatment efficiency, (ii) multi-activity assessment using various organics, (iii) electron paramagnetic spectral

(EPR) features, and (iv) intermediate distributions. Together with post-mortem analysis of spent anodes, the practical applicability during the prolonged operation was probed by monitoring the reduction in treatment performance while the conductive titanium oxides were applied for repeated anodic oxidation in distilled water and real flue gas desulfurization (FGD) wastewater, and under continuous operation mode.

2. Materials and methods

2.1. Chemical reagents

The reagents used in this study include acetaminophen (ACT; Sigma-Aldrich), benzoic acid (BA; Sigma-Aldrich), bisphenol A (BPA; Sigma-Aldrich), carbamazepine (CBZ; Sigma-Aldrich), 4-chlorophenol (4-CP; Sigma-Aldrich), nitrobenzene (NB; Sigma-Aldrich), 4-nitrobenzoic acid (4-NBA; Sigma-Aldrich), tetracycline (TER; Sigma-Aldrich), methanol (MeOH; J.T. Baker), *tert*-butanol (*t*-BuOH, Sigma-Aldrich), formaldehyde (HCHO; Sigma-Aldrich), hypochlorous acid (HOCl; Sigma-Aldrich), peroxydisulfate (PDS; Sigma-Aldrich), ethylene glycol (EG; Sigma-Aldrich), 5-*tert*-butoxycarbonyl 5-methyl-1-pyrroline-*N*-oxide (BMPO; ENZO Life Sciences, Inc.), 2,4-dinitrophenylhydrazine (DNPH; Sigma-Aldrich), *N*, *N*'-diethyl-*p*-phenylenediamine (DPD; Sigma-Aldrich), ammonium fluoride (AF; Sigma-Aldrich), potassium phosphate monobasic (Sigma-Aldrich), perchloric acid (Sigma-Aldrich), sulfuric acid (Junsei), sodium hydroxide (Sigma-Aldrich), sodium sulfate (Sigma-Aldrich), sodium chloride (Sigma-Aldrich), and acetonitrile (J.T. Baker). All chemicals were used without further purification. The experimental solutions were prepared using ultrapure deionized water (DI) (>18 M $\Omega\cdot\text{cm}$), produced from a Milli-Q Water Purification System (Millipore).

2.2. Preparation and characterization of TiO_2 -derived anodes

Anatase TiO_2 (A- TiO_2) NTA was produced by anodizing a rectangular 1 cm \times 3 cm titanium (Ti) plate with a thickness of 1 mm in 30 mL mixture consisting of EG, AF, and DI in the volume ratios 97.3:0.2:2.5, according to the method described elsewhere [34,35]. Nanotube growth was performed at 10 $^\circ\text{C}$ via a two-step anodization process in which Ti plate was treated at 45 V for 5 h, and subsequently at 10 V for 5 min. Ti plate and Pt foil with the same dimensions served as the anode and cathode, respectively, and were placed in parallel with an inter-electrode gap of 1 cm. Potential difference was applied using a DC power supply (E3647A; Keysight Technologies). The resultant amorphous TiO_2 NTA was subjected to thermal annealing at 450 $^\circ\text{C}$ for 1 h, crystallizing to anatase counterpart. Magnéli phase NTAs were fabricated by annealing A- TiO_2 NTA in an atmosphere of H_2/N_2 mixture (in the ratio of 1:5) at 108 sccm at temperatures ranging from 650 to 850 $^\circ\text{C}$ [23]. Note that Magnéli phase production via hydrogen annealing was performed at the temperatures above 600 $^\circ\text{C}$ where anatase-to-rutile phase transformation is initiated because the transition of anatase to Magnéli phase typically involves the formation of rutile phase as the intermediate [36]. B- TiO_2 NTA was prepared by electrochemical reduction of A- TiO_2 NTA in 0.1 M phosphate buffer at the fixed current density of 17 mA cm^{-2} for 90 s [37]. Cathodization was conducted in two-electrode setup, in which A- TiO_2 NTA and Pt foil of the same size acted as the cathode and anode, respectively, and were positioned side by side with inter-electrode spacing of 10 mm.

Surface morphological characteristics of the pristine and thermally/electrochemically reduced A- TiO_2 NTAs were identified using field emission scanning electron microscopy (FE-SEM; FEI Quanta FEG 250). The phase transition of TiO_2 NTA via post-treatment processes, i.e., thermal reduction and cathodization, was explored by X-ray diffraction (XRD; Rigaku SmartLab) using Cu-K α radiation. The change in the oxidation states of Ti and oxygen that occurs by Ti^{3+} and OV introduction was probed by X-ray photoelectron spectroscopy (XPS;

ULVAC-PHI) using a monochromatic Al-K α X-ray source (140.00 eV) (detection depth of ~ 7 nm). The occurrence of OV_s (or Ti³⁺ states) was further investigated based on the Raman spectra recorded by LabRam ARAMIS Raman spectrometry (Horiba Jobin-Yvon) using an argon ion laser with excitation at 514.5 nm, EPR spectra obtained using a Bruker EMX Plus spectrometer operating at 100 kHz field modulation, and X-ray absorption spectra (XAS) acquired at the Ti *L*-edge and O *K*-edge in total electron yield mode. The XAS measurements were conducted at the 8A1 beamline of the Pohang Accelerator Laboratory, Pohang, South Korea.

2.3. Electrochemical measurements

The electrochemical properties of A-TiO₂ NTA and its reduced counterparts were analyzed by CV and EIS. The electrochemical measurements were conducted in a two-compartment cell with a three-electrode configuration (in which TiO₂-derived NTA, Ag/AgCl, and Pt coil served as the respective working, reference, and counter electrodes) and reaction parameter control and electrochemical response monitoring were performed using a potentiostat (Ivium-n-Stat, Ivium Technologies or SP-300 bipotentiostat, Biologic Science Instruments). Nyquist plots were obtained in 0.1 M Na₂SO₄ solutions at the applied potential of 2.5 V vs. Ag/AgCl with an amplitude of 10 mV over the frequency range of 100 kHz to 100 mHz. Mott-Schottky analysis was conducted in 0.5 M Na₂SO₄ solutions at a frequency of 100 Hz. SECM was performed on an M470 workstation equipped with SP-300 bipotentiostat (Biologic Science Instruments). The Pt ultramicroelectrode (UME, Biologic Science Instruments) with a diameter of 10 μ m, and radius ratio of glass sheath to UME of 10 was employed as a sensing tip under working electrolyte volume of 8 mL. The local CIER activity was visualized in the sample generation/tip collection mode of SECM with the respective potentials of substrate and tip initially set to 3.0 V and -0.6 V vs. Ag/AgCl in 0.5 M NaCl solutions. The tip potential for chlorine reduction reaction was determined by the CVs of the conductive Ti₄O₇ NTA (Fig. S1a). Prior to areal scans, tip-to-substrate distance (*d*) was identified by approach curve in 1 mM FcMeOH + 100 mM KCl, fitted to the theoretical model (Fig. S1b) [38]. The tip was scanned along the area of 100 μ m \times 50 μ m with step size of 5 μ m per point and step velocity of 10 μ m s⁻¹ at nominal *d* of ~ 3 μ m. Conductivity measurements were performed for the fresh and spent samples in the feedback mode of SECM as the tip at 0.4 V vs. SCE was approached to each sample under open-circuit condition with a step size of 2 μ m per point and step velocity of 10 μ m s⁻¹ in 1 mM FcMeOH + 100 mM KCl. For two-point solid-state measurements, a gold counter electrode with the active area of 0.16 cm² was deposited on conductive TiO₂-derived NTAs by thermal evaporation, and the resistance estimated from the I-V characteristics was measured using a potentiostat. Anodic stability was evaluated based on the time-dependent potential variation during the prolonged electrolysis with Ti₄O₇ and B-TiO₂ for 100 h at a fixed current density of 5 mA cm⁻².

2.4. Experimental procedures and analytical methods

Anodic oxidation of organic compounds was performed in a magnetically stirred 50 mL undivided batch reactor in either constant voltage or constant current density mode. Voltage and current density in the range of 2–4 V vs. Ag/AgCl and 2.5–10 mA cm⁻², respectively, were applied to the electrode couples using a DC power supply (E3647A; Keysight Technologies). Electrochemical oxidation proceeded in the aqueous solutions that typically contained 0.1 mM target substrate and 0.5 M Na₂SO₄ or NaCl as the supporting electrolyte with a two (or three)-electrode system where TiO₂-derived anode was paired with Ti plate or Pt coil as the cathode (or Ag/AgCl as the reference electrode). Initial and residual concentrations of organic compounds were monitored by high-performance liquid chromatograph (HPLC, Agilent infinity 1260) equipped with a UV/Vis detector (G1314F 1260VWD) and a

C-18 column (ZORBAX EclipseXDB-C18). The extent of organic mineralization was quantified based on total organic carbon (TOC) loss determined by a TOC analyzer (TOC-L CPH/CPN, Shimadzu). The concentrations of HOCl and PDS as secondary non-radical oxidants were measured by colorimetric methods based on DPD and iodide oxidation, respectively; Würster dye and iodine as the major oxidation products were spectrophotometrically quantified at the respective wavelengths of 515 nm [39] and 352 nm [40]. HCHO concentration was determined by HPLC analysis subsequent to derivatization with DNPH. To identify oxidizing radicals generated via anodic oxidation, the EPR spectra were recorded by JESTE 300 spectrometry (JEOL) in the presence of BMPO as a spin trap under the following operating conditions: microwave power = 1 mW, microwave frequency = 9.4136 GHz, center field = 3350 G, modulation width = 0.2 mT, and modulation frequency = 100 kHz.

3. Results and discussion

3.1. Characteristics of thermally and electrochemically reduced TiO₂ NTAs

A cross-sectional SEM image of A-TiO₂ NTA (Fig. S2a) shows close-packed bundles of TiO₂ nanotubes of approximately 5 μ m in length aligned vertically on Ti substrate. Uniformly distributed pores presented in the top surface image displayed the inner diameter of ~ 60 nm (Fig. S2d). Hydrogen annealing and cathodization intended to induce phase transformation and Ti³⁺ self-doping, respectively, marginally changed the geometrical features of TiO₂ NTA with highly ordered periodicity (Fig. S2b–c and e–f). Multiple XRD fingerprint peaks (JCPDS card no. 21–1272) that indicated the selective formation of anatase phase (without anatase-to-rutile transition) through the annealing of anodized Ti plate at 450 °C emerged in the diffraction pattern of A-TiO₂ NTA (Fig. 1a). The subsequent cathodization maintained the characteristic diffraction pattern intact but reduced the peak intensity, which typically occurred upon Ti³⁺ implantation in TiO₂ [20]. Only B-TiO₂ prepared under optimal condition was characterized, because the activity of the B-TiO₂ samples for anodic oxidation was almost insensitive to the fabrication conditions (i.e., the applied current and cathodization time) (Fig. S3). Monitoring of the XRD patterns in the range of annealing temperature from 650 to 850 °C implied that heat treatment in a hydrogen atmosphere initiated the phase conversion from anatase to Magnéli at 700 °C, and the extent of Ti⁴⁺ reduction steadily increased with increasing temperature. MP-700 NTA (Magnéli phase produced via hydrogen annealing at 700 °C; the three digits next to MP indicate the temperature) displayed the XRD peaks unique to Ti₄O₇ (e.g., peaks at $2\theta = 20.7$ and 31.7° indexed to the lattice planes of (1 0 -2) and (1 0 -4), respectively [23]), along with the diffraction features corresponding to Ti₈O₁₅ and Ti₆O₁₁. Ti₄O₇ became dominant over the other Magnéli phases at 750 °C (MP-750 NTA is referred to as Ti₄O₇ NTA hereafter, accordingly) and as temperature further increased, transformed into titanium suboxides with the relatively low-valence Ti species, such as Ti₃O₅, Ti₂O₃, and TiO (detected in MP-800 and MP-850 NTAs). This was compatible with the trend of titanium suboxides with the lower Ti valence states readily occurring under the higher temperature conditions, often observed in the literature [41]. Raising temperature renders surface oxygen atoms vibrate in a more intense way and thus susceptible to release from the lattice when metal oxides are exposed to reducing agents [42]. Accordingly, hydrogen annealing at the higher temperatures should favor the formation of Magnéli phases having lower Ti/O ratios.

Slight peak shifting toward lower binding energy in the Ti 2p XPS spectrum was observed after cathodic polarization of A-TiO₂ (Fig. 1c), confirming the occurrence of Ti³⁺ state [36,43]. Aligned with universal Ti/O ratio variation, thermal hydrogenation more significantly displaced a Ti 2p doublet pair (i.e., Ti 2p_{1/2} and Ti 2p_{3/2} peaks) toward lower binding energy (Fig. 1b). Surface Ti³⁺ content steadily increased with increasing annealing temperature and varied from 5.74 to 46.45 at

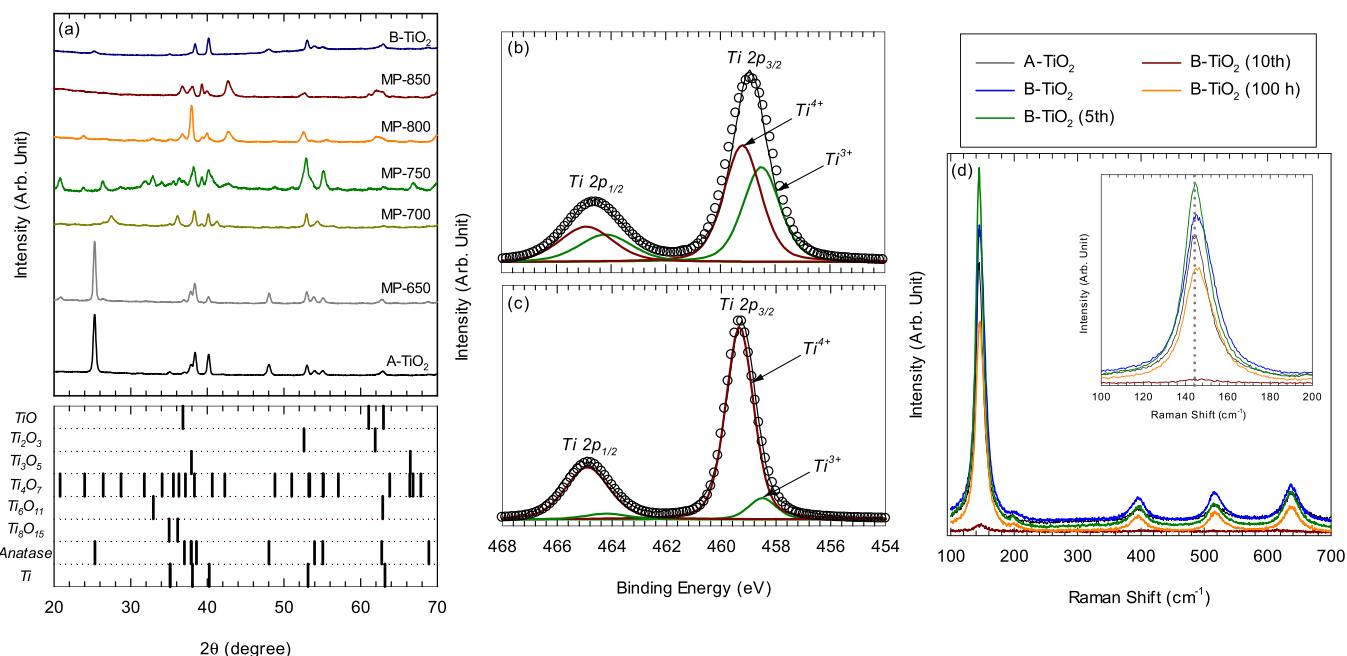


Fig. 1. (a) XRD patterns of Magnéli phases and B-TiO₂ (three-digit numbers next to MP indicate annealing temperatures), XPS spectra of (b) Ti₄O₇ and (c) B-TiO₂, and (d) Raman spectra of the fresh and spent B-TiO₂ (obtained after prolonged or repeated anodic oxidation (operation time or the number of catalytic cycles was specified in the sample names)). Inset shows the expanded Raman spectra in the wavenumber range of 100–200 cm⁻¹.

%, according to surface chemical compositions estimated by peak deconvolution of the XPS spectra (Table S1 and Figs. 1b-c and S4). This aligned with the temperature-dependent change in the surface atomic percentage of OV (formed to compensate the charge imbalance caused by Ti³⁺ self-doping) computed from the intensity of the XPS peak at 531.8 eV in the deconvoluted O 1s XPS spectra (Fig. S5). Three main peaks at 529.9, 531.8, and 532.6 eV correspond to lattice oxygen surface-bound to Ti⁴⁺ (Ti-O), adsorbed oxygen, and hydroxyl group, respectively [44,45]. Since adsorbed oxygen species undergo dissociative adsorption to fill and stabilize OVs, their content is quantitatively correlated with the relative OV concentration [9,44,45]. The contents of Ti³⁺ and OV as a function of annealing temperature linked up with the diffraction patterns of Magnéli phases, obtained by the XRD measurements with a typical penetration depth of 5–10 μm (Fig. 1a). However, it should be noted that the atomic percentage of Ti³⁺ (or OV) species, determined based on the XPS data acquired from the top few nanometers of the surface, is unlikely to reflect the bulk chemical composition of B-TiO₂ because cathodic polarization generates Ti³⁺ (or OV) states in the subsurface region of TiO₂, although the relative peak intensity of the Ti 2p XPS spectra has been used to estimate the variation in Ti³⁺ content or Ti³⁺/Ti⁴⁺ ratio [46]. Ti³⁺ formation by electrochemical self-doping was further supported by noticeable blue shift and broadening of Raman peak at 144.4 cm⁻¹ (Fig. 1d) [20].

The EPR peaks corresponding to the paramagnetic Ti³⁺ species and OVs (concurrently formed to maintain electrical neutrality) at $g = \sim 1.940$ and 2.004 , respectively, typically occurred for titanium oxides with oxygen non-stoichiometry [47]. A strong EPR signal at $g = \sim 2.004$ was observed exclusively for Ti₄O₇ whereas any detectable spectral features assignable to Ti³⁺ and OV states barely formed for A-TiO₂ and self-doped TiO₂ (Fig. S6a). Since the EPR peak at $g = \sim 2.004$ was suggested to be associated with O₂⁻ species formed via single-electron reduction of surface-adsorbed O₂ by Ti³⁺ [32], the EPR detection of OV alone may suggest the possibility that Ti³⁺ existed primarily in the subsurface region of Ti₄O₇ (note that selective Ti³⁺ occurrence in the EPR spectra implies that Ti³⁺ concentrates in the bulk in the same sense) [48].

3.2. Electrochemical properties of TiO₂-derived anodes

The Nyquist plots for Magnéli phases showed a volcano-type correlation between annealing temperature and electrocatalytic activity based on the charge-transfer resistance (R_{ct}) that is quantitatively related to the diameter of semicircle (Table S2). Hydrogen annealing at 750 °C produced the most conductive titanium suboxide (i.e., Ti₄O₇), while further increasing or decreasing temperature gradually retarded the interfacial charge transfer over Magnéli phases (Figs. 2a and S7). The result conformed to the relative conductivity of Magnéli phases (Ti_nO_{2n-1} with $n = 3, 4$, or 5 , such as Ti₄O₇ and Ti₃O₅, is highly conductive) [16]. Cathodic reduction as a facile approach to fabricate B-TiO₂ from A-TiO₂ by introducing Ti³⁺ defects in the lattice of TiO₂ drastically shrunk the semicircle in the Nyquist plot, which suggested substantial improvement in the electrochemical properties via self-doping, but the comparison in terms of R_{ct} value implied that Ti₄O₇ possessed higher potential as anode material than B-TiO₂. The I-V characteristics obtained by two-point solid-state measurements also supported that the non-stoichiometry of Ti/O ratio led to drastic increase in electrical conductivity of the pristine TiO₂ (inset of Fig. 2b). Together with the lowest resistance (R) of Ti₄O₇ ($R = 62.77, 4.37$, and $0.18 \Omega \text{ cm}^{-2}$ for A-TiO₂, B-TiO₂, and Ti₄O₇ NTAs, respectively), it exhibited a linear I-V relationship (represented by a straight line with positive slope) typically observed for conductors, whereas the J-shaped I-V graphs for B-TiO₂ and MP-700 indicated their semi-metallic nature [9]. These findings substantiated that the electrical conductivity was primarily responsible for the electrocatalytic performance of the conductive TiO₂-derived anodes. The OV content of Magnéli phases, estimated based on the EPR peak intensity (Fig. S6b), likely aligned with their temperature-dependent electric conductivity (Fig. 2a). The quantity of OV species as a key for the electrocatalytic activity of titanium suboxides increased in proportion to annealing temperature, was maximized at 750 °C (for Ti₄O₇), and declined as temperature was further raised.

To quantitatively explore variation in the electrical conductivity of TiO₂ upon hydrogen annealing and cathodization, A-TiO₂, Ti₄O₇, and B-TiO₂ NTAs were compared in terms of charge carrier density (N_D) computed from the slopes of Mott-Schottky plots (details in N_D

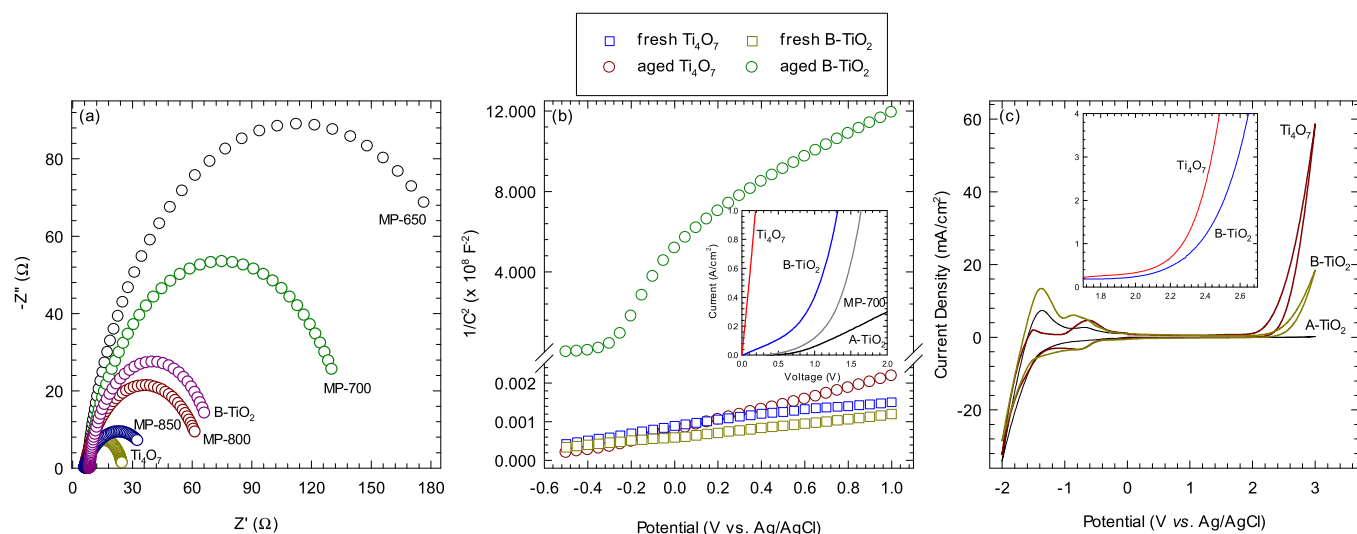


Fig. 2. (a) Nyquist plots for Magnéli phases and B-TiO₂, (b) Mott-Schottky plots for fresh and aged Ti₄O₇ and B-TiO₂, and (c) CVs obtained in 0.5 M Na₂SO₄ solutions for A-TiO₂, Ti₄O₇, and B-TiO₂. Insets of b and c show I-V characteristics and CVs obtained in 0.5 M NaCl solutions, respectively.

determination are described in Text S1) (Figs. 2b and S8). Whereas A-TiO₂ as the intrinsic semiconductor exhibited the lowest carrier concentration ($4.04 \times 10^{18} \text{ cm}^{-3}$), anatase-to-Magnéli transformation and electrochemical self-doping caused a 5–6 order of magnitude improvement in carrier density (it should be noted that the N_D value served as an indicator to comparatively assess the TiO₂-derived anodes in terms of electrical conductivity in a qualitative way, because the Mott-Schottky equation used to derive N_D is proper to characterize the electrocatalytic behaviors of the planar electrodes [49]). Consistent with the measured electrochemical properties (Fig. 2a), Ti₄O₇ was more electrically conductive than B-TiO₂, with $N_D = 1.68 \times 10^{24}$ and $7.01 \times 10^{23} \text{ cm}^{-3}$ for Ti₄O₇ and B-TiO₂ NTAs, respectively.

Voltammetric characteristics of A-TiO₂, Ti₄O₇, and B-TiO₂ NTAs indicated that hydrogen annealing and cathodization improved the capacitance of A-TiO₂ and lowered the overpotentials for oxygen and hydrogen evolution via water splitting (Fig. 2c). In the voltammogram for Ti₄O₇ NTA, a reduction peak occurred at $\sim -0.75 \text{ V}$ while the potential was negatively scanned and the equivalent oxidation peak emerged at $\sim -0.60 \text{ V}$ during the reverse scan. The redox peaks resulted from the surface reduction and reoxidation of Ti₄O₇ phase occurred at ~ -0.75 and -0.60 V , respectively [23]. The CV curve of B-TiO₂ NTA showed the peak at $\sim -0.70 \text{ V}$ that arises from the proton intercalation to accomplish charge balance during $\text{Ti}^{3+}/\text{Ti}^{4+}$ redox reaction (Ti^{4+} -to- Ti^{3+} reduction during the cathodic reduction of TiO₂ involves proton insertion in the lattice) [50]. In particular, Ti₄O₇ NTA exhibited lower onset potentials for CLER and OER (estimated from the interactions between baseline and the tangents to the rising currents in the anodic scan of CVs obtained at excess chloride and sulfate), compared to B-TiO₂ NTA (Fig. 2c and its inset), principally due to lower ohmic drop. Performance tests using Magnéli phases prepared at different annealing temperatures (Fig. S9) indicated that the efficiencies for CLER and anodic 4-CP degradation were positively correlated with electrical conductivity.

3.3. Comparative assessment for anodic oxidation reactions

The relative position of Ti₄O₇ NTA against B-TiO₂ NTAs was identified based on the anodic efficiencies of (i) HOCl production, (ii) MeOH-to-HCHO conversion, and (iii) 4-CP degradation under varying voltage conditions (Fig. 3). HOCl concentration steadily increased within the timeframe of 20–30 min, reaching the saturation points, regardless of anode type and applied voltage (Fig. S10). The maximal CLER efficiency of Ti₄O₇ NTA (determined from temporal changes in anodic HOCl

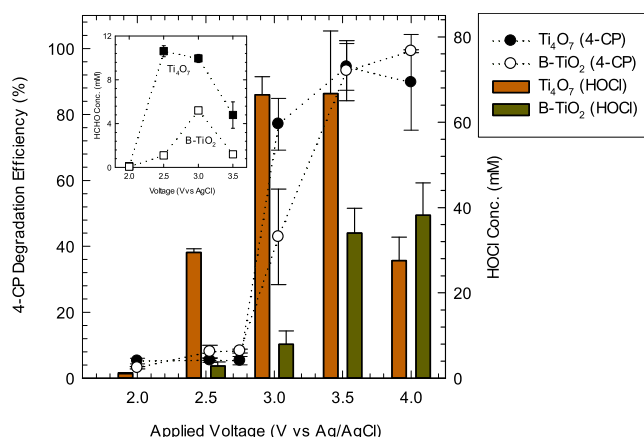


Fig. 3. Comparison of Ti₄O₇ and B-TiO₂ in terms of chlorine evolution and anodic oxidation of MeOH and 4-CP under varying voltage conditions ([4-CP]₀ = 0.1 mM; [MeOH]₀ = 200 mM; [Na₂SO₄]₀ = 0.5 M (or [NaCl]₀ = 0.5 M for chlorine evolution); pH_i = 5). Inset shows the maximum concentration of HCHO formed via MeOH oxidation.

production in Fig. S10) displayed a volcano-type dependence on applied voltage (undergoing decline after reaching a plateau). In contrast, the maximum HOCl production continued to increase in proportion to voltage when B-TiO₂ was used as anode instead, although the rate of increase slowed under the high voltage conditions. Aligned with the higher electrical conductivity and lower onset potential for CLER (Fig. 2), Ti₄O₇ NTA outperformed B-TiO₂ NTA in anodic HOCl formation over a voltage range of 2.5–3.5 V. It is noteworthy that the electrocatalytic activity of Ti₄O₇ NTA for CLER at 2.5 and 3.0 V was higher than that of B-TiO₂ NTA by a factor of 7–8. Local electrochemical activity for CLER, visualized in the SECM areal scan images, also confirmed the higher yield of Ti₄O₇ for anodic HOCl production (Fig. S11). According to the color change from blue to red that indicated the increased CLER current at tip, the observation on the broader distribution of red-colored area over the scanned Ti₄O₇ anode supported that Ti₄O₇ was more electrocatalytically active for HOCl generation than B-TiO₂.

The reduction in the electrocatalytic performance of Ti₄O₇ after the highest CLER efficiency was achieved at $\sim 3.5 \text{ V}$ was possibly attributed to (i) cathodic HOCl reduction and (ii) further oxidation into the chlorine oxyanions (e.g., ClO_2^- and ClO_3^-) under the relatively high voltage

conditions. The trend of the electrocatalytic activity of Ti_4O_7 declining at 4 V after reaching the maximum point was still observed in the experiments conducted using a two-compartment cell that prevented HOCl from transforming back into Cl^- via cathodic reduction (Fig. S12). Even B- TiO_2 exhibited the similar voltage-dependent HOCl production (note that increasing the applied voltage from 3.5 to 4.0 V did not decrease the maximum CIER efficiency of B- TiO_2 (Fig. 3), even though HOCl concentration, measured as a function of electrolysis time at 4.0 V in an undivided cell, continued to decline after reaching the maximum and eventually stood at the lower level than HOCl concentration monitored at 3.5 V (Fig. S10)). This ruled out the possibility that electrocatalytic reduction promoted at the higher applied voltages could lower the overall efficiency of Ti_4O_7 for anodic HOCl production. Monitoring of chlorine oxyanions during anodic Cl^- oxidation under varying voltage conditions showed that further oxidation of HOCl into ClO_2^- , ClO_3^- , and ClO_4^- more significantly proceeded as the applied voltage increased (Fig. S13). Therefore, the observed reduction in the CIER efficiency at 4 V may be ascribed to the enhanced oxidative conversion of HOCl into the corresponding oxyanions under the higher voltage conditions. However, further study is required for proper explanation on the dependence of CIER on the applied voltage.

HCHO production was monitored with increasing applied voltage when Ti_4O_7 and B- TiO_2 NTAs were applied for anodic MeOH oxidation at excess sulfate-based electrolyte (Fig. S14). The oxidative conversion of MeOH to HCHO proceeded primarily through $\bullet\text{OH}$ -induced hydrogen-atom abstraction [51]. The possibility of direct anodic oxidation and indirect oxidation by sulfate radical ($\text{SO}_4^{\bullet-}$) generated from sulfate via single-electron transfer [52] was ruled out, based on (i) no occurrence of anodic peaks corresponding to the direct MeOH and sulfate oxidation in CV (Fig. S15), (ii) marginal PDS formation due to $\text{SO}_4^{\bullet-}$ recombination [52] (Fig. S16), and (iii) EPR spectral features indicating exclusive $\bullet\text{OH}$ formation (Fig. 4c). Ti_4O_7 NTA exhibited better performance in anodic oxidation than B- TiO_2 NTA over the entire applied voltage range based on the maximum HCHO yield (obtained from Fig. S14) (inset of Fig. 3).

A comparison of electrocatalytic activity for oxidative 4-CP treatment (assessed based on the efficiency of anodic 4-CP degradation as a function of applied voltage (Fig. S17)) showed no significant difference between Ti_4O_7 and B- TiO_2 NTAs (Fig. 3), though the superiority of Ti_4O_7 over B- TiO_2 was marked at 3.0 V. The result that contrasted with the anodic activity of Ti_4O_7 for HOCl production and MeOH oxidation being higher than that of B- TiO_2 may be attributed to direct oxidation pathway preferentially induced on B- TiO_2 NTA. The oxidation peak (arising from

direct electron transfer from 4-CP to the anode) at ~ 1.4 V vs. Ag/AgCl [53] in the anodic scan of CV, which gradually increased with increasing 4-CP concentration, occurred for B- TiO_2 NTA, whereas the anodic peak was absent for Ti_4O_7 NTA, regardless of 4-CP concentration (Fig. S18).

3.4. Primary reaction pathways for anodic organic degradation

To explore the contribution of $\bullet\text{OH}$ to anodic organic oxidation, 4-CP degradation during electrolysis with Ti_4O_7 and B- TiO_2 NTAs in constant current mode was performed in the presence of excess alcohol-based radical scavengers, i.e., MeOH and *t*-BuOH (Fig. 4a). Monitoring of temporal voltage variation at fixed current density of 5 mA cm^{-2} (set for all the mechanistic studies) showed that voltage measured with B- TiO_2 more sharply increased with electrolysis time, reaching the higher saturation level (Fig. S19). This implied that anodic oxidation was initiated at the lower applied voltages when Ti_4O_7 was used instead of B- TiO_2 for constant-current electrolysis. Thus, the observed anodic efficiency gap between the two OV-rich Ti-based anodes could contrast with the superiority of Ti_4O_7 NTA over B- TiO_2 , which was confirmed by performance tests under constant voltage conditions. For both TiO_2 -derived anodes, the kinetic rate anodic 4-CP oxidation was drastically retarded upon alcohol addition, suggesting the role of $\bullet\text{OH}$ as the major oxidant. Multi-activity assessment using eight organic substrates, such as ACT, BA, BPA, CBZ, 4-CP, NB, 4-NBA, and TER, also confirmed that $\bullet\text{OH}$ served as the dominating reactive species (Figs. 4b and S20). The anodic efficiency of Ti_4O_7 and B- TiO_2 NTAs for organic degradation did not significantly vary depending on which compound was chosen as a model substrate, which accorded with the non-selective reactivity of $\bullet\text{OH}$. Despite the higher OER potential of B- TiO_2 NTA that was likely to favor anodic $\text{SO}_4^{\bullet-}$ formation (Fig. 2c), NB and 4-NBA that exhibit a strong resistance to oxidation by $\text{SO}_4^{\bullet-}$ ($k(\text{NB}) = k(4\text{-NBA}) \leq 10^6 \text{ M}^{-1} \text{ s}^{-1}$ [54]) effectively decomposed on both anodes, which ruled out that $\text{SO}_4^{\bullet-}$ contributed to anodic organic oxidation at excess sulfate-based electrolyte. The electrolyte exchange from sulfate to chloride caused a transition in the major oxidant from $\bullet\text{OH}$ to HOCl with substrate-specific reactivity. Anodic oxidation of BA, NB, and 4-NBA slowly proceeded during electrolysis at excess chloride whereas ACT, BPA, CBZ, 4-CP, and TER completely decomposed within 30 min (Fig. S21).

The distribution of intermediates generated during anodic oxidation of ACT, BA, and 4-CP further confirmed no marked difference in the main degradative pathway between Ti_4O_7 and B- TiO_2 (Tables S3–S5). Whereas intermediates unique to either Ti_4O_7 or B- TiO_2 NTA were

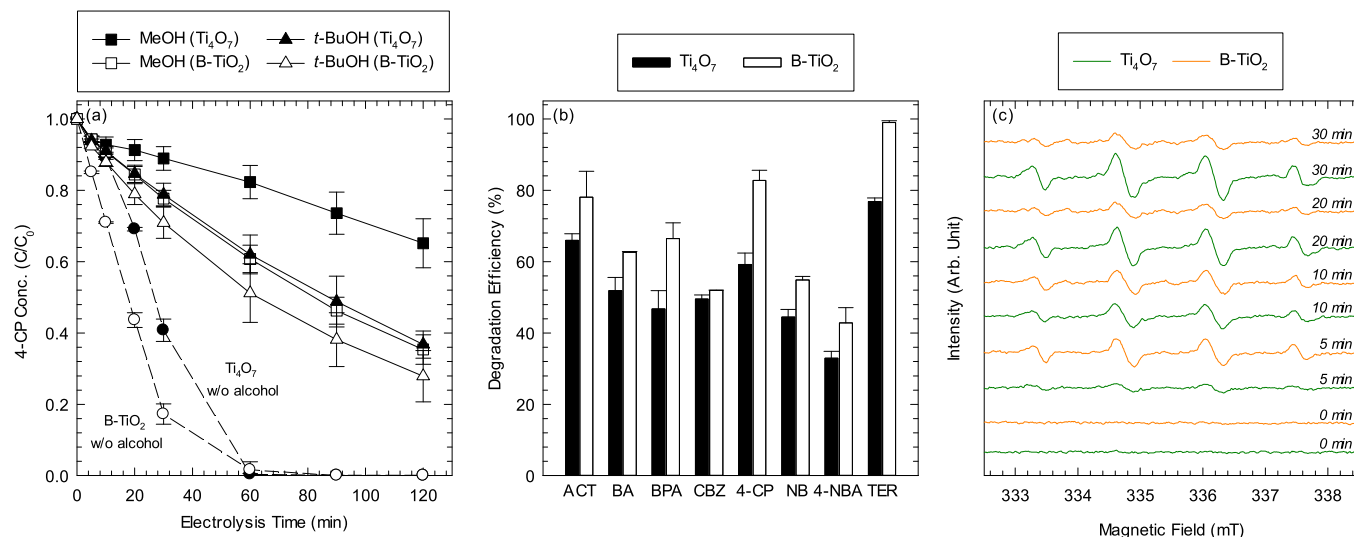


Fig. 4. (a) Effect of alcohol-based scavengers on the rate of anodic 4-CP oxidation, (b) multi-activity assessment using diverse organics, and (c) EPR spectra features of Ti_4O_7 and B- TiO_2 (current density = 5 mA cm^{-2} ; $[\text{organic compound}]_0 = 0.1 \text{ mM}$; $[\text{MeOH}]_0 = [\text{t-BuOH}]_0 = 0.1 \text{ M}$; $[\text{BMPO}]_0 = 10 \text{ mM}$; $[\text{Na}_2\text{SO}_4]_0 = 0.5 \text{ M}$; $\text{pH}_i = 5$).

scarcely detected, the majority of intermediates formed via $\bullet\text{OH}$ -induced hydroxylation and ring-opening reactions commonly occurred: mono-hydroxybenzoic acid isomers (e.g., salicylic acid) and maleic (or fumaric) acid for BA and dihydroxybenzoquinone, chlorobenzene-diol, and maleic/succinic acid for 4-CP. In addition to some multihydroxylated intermediates, nitrophenols, typically detected during ACT oxidation by $\bullet\text{OH}$ [55,56], also occurred for both TiO_2 -derived anodes. Along with the extent of TOC reduction (evidencing organic mineralization) as a function of current density (Fig. S22), the EPR spectral features monitored with electrolysis time (Fig. 4c) corroborated that the electrocatalytic

activity for $\bullet\text{OH}$ production enabled anodic organic treatment by Ti_4O_7 and B- TiO_2 NTAs.

3.5. Long-term stability evaluation

The practical application of Ti_4O_7 and B- TiO_2 NTAs for anodic water treatment was explored based on the extent of electrocatalytic activity loss during repeated 4-CP degradation over 10 cycles (Fig. 5a). Prior to each run, spent anodes were rinsed out multiple times with distilled water and immersed in fresh experimental solutions. The used B- TiO_2

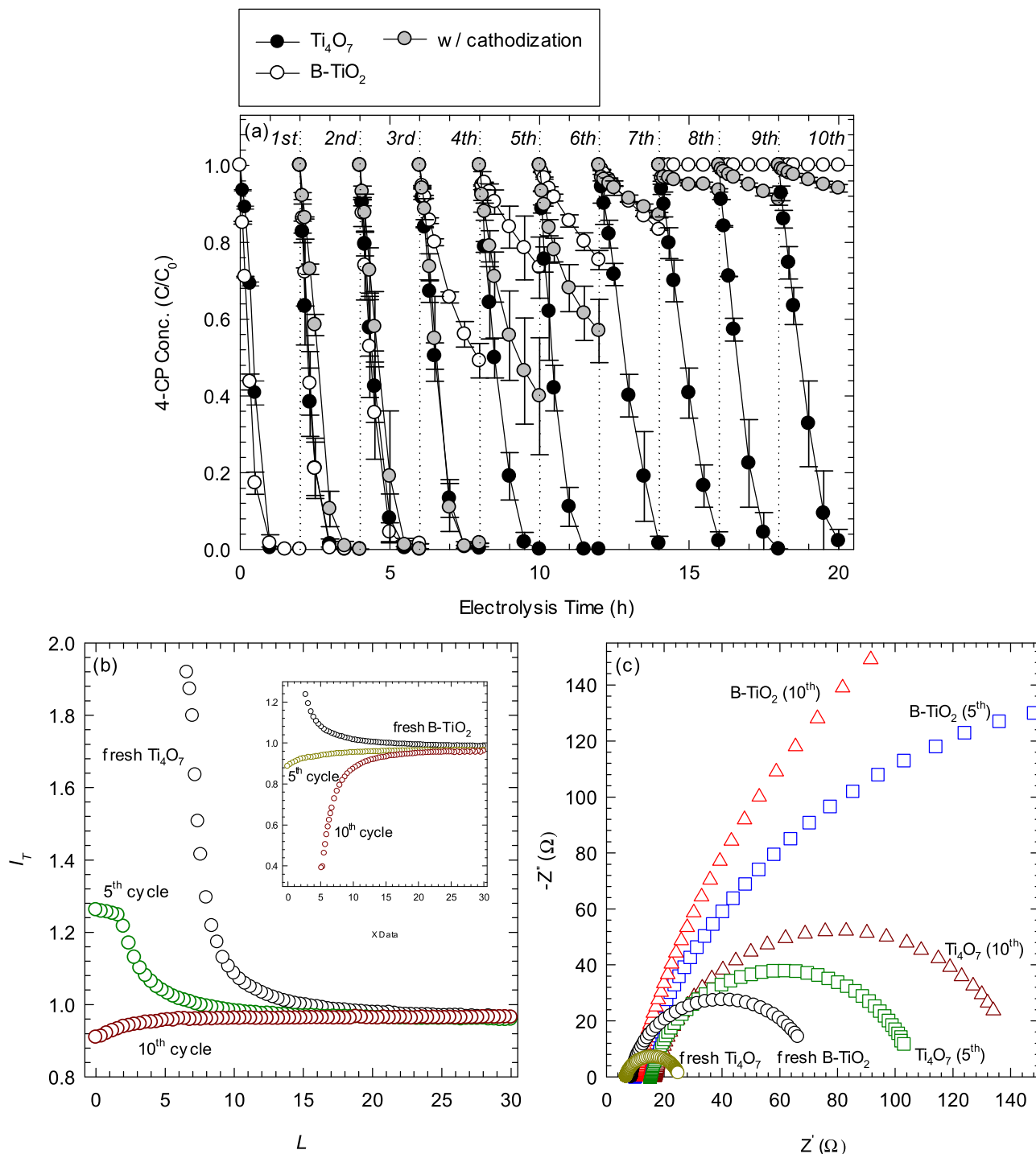


Fig. 5. (a) Repetition test (current density = 5 mA cm^{-2} ; $[\text{4-CP}]_0 = 0.1 \text{ mM}$; $[\text{Na}_2\text{SO}_4]_0 = 0.5 \text{ M}$; $\text{pH}_i = 5$), (b) approach curves of the fresh and used Ti_4O_7 and B- TiO_2 (I_T and L indicate normalized tip current (i_T/i_∞) and normalized distance between tip and sample (d/a ; a: Pt UME tip radius), respectively), and (c) Nyquist plots for the fresh and used Ti_4O_7 and B- TiO_2 .

NTA was subjected to cathodization to regenerate Ti^{3+} after every run. Otherwise, only three cycles of anodic oxidation halved the electrocatalytic activity of B-TiO₂. Treatment efficiency of B-TiO₂ NTA remained constant through four consecutive runs, gradually declined over five to seven repetitive cycling, and fell to almost zero level after the seventh cycle. In contrast, Ti₄O₇ NTA was barely deactivated while repeatedly used 10 times for anodic oxidation. This conformed to the chemical stability of Ti₄O₇ phase [16], implying that Ti₄O₇ is more suited for prolonged operation than B-TiO₂. The superior durability of Ti₄O₇ was further confirmed in the repetition tests conducted in the sulfate-laden real FGD wastewater spiked with 0.1 mM 4-CP (Fig. S23) (without external supply of sulfate-based electrolyte). Ten cycles of anodic oxidation led to the minor deactivation of Ti₄O₇ NTA whereas B-TiO₂ NTA became electrochemically inert after undergoing gradual activity loss over three cycles.

Variation in the electrochemical properties of Ti₄O₇ and B-TiO₂ NTAs during multiple use aligned with the superiority of Ti₄O₇ over B-TiO₂ in repeated anodic oxidation. The extent of N_D reduction determined according to the Mott-Schottky equation after the 10th cycle was more pronounced for B-TiO₂, with $N_D = 7.01 \times 10^{23}$ and $2.47 \times 10^{19} \text{ cm}^{-3}$ for fresh and spent B-TiO₂ versus $N_D = 1.68 \times 10^{24}$ and $1.07 \times 10^{24} \text{ cm}^{-3}$ for fresh and spent Ti₄O₇ (Figs. 2b and S8). The comparison of current response of the Pt UME tip approaching the fresh and spent anodes in the positive feedback mode of SECM, quantitatively correlated with local conductivity [57,58], indicated that the conductivity of Ti₄O₇ varied with increasing catalytic cycle to a much less extent than that of B-TiO₂ (Fig. 5b). Nyquist plots for TiO₂-derived anodes generated after the 5th and 10th cycles further supported that the used Ti₄O₇ samples exhibited higher electrical conductivity than the B-TiO₂ counterparts (Fig. 5c). The relative stability during prolonged run was evaluated based on temporal change in the potential of Ti₄O₇ and B-TiO₂ during 100-h electrolysis at fixed current density (Fig. S24). Consistent with the observation that B-TiO₂ was more prone to deactivation than Ti₄O₇, a steeper potential rise within the shorter timeframe occurred for B-TiO₂. Further, the SEM images of B-TiO₂ samples obtained after repeated anodic oxidation-cathodic polarization cycles showed the significant collapse of the nanotubular structures (NTAs were peeled off from the Ti plates and some nanotubes were shortened (Fig. S25a-b and d-e)), which was in marked contrast to the observation that the aligned NTA configuration of Ti₄O₇ samples remained undamaged (Fig. S25c and f). Reoxidation of Ti^{3+} to Ti^{4+} , associated with the steady loss of the electrocatalytic activity of B-TiO₂ during repeated anodic oxidation, was supported by the Raman peak shift observed with the spent B-TiO₂ samples (inset of Fig. 1c). The peak at 144.4 cm^{-1} , shifted toward higher wavenumber due to Ti^{3+} formation, was displaced to the original position. However, the spectral characteristics, such as the relative intensity ratio of e_g and t_{2g} peaks, which are quantitatively correlated with Ti^{3+} and OV contents [59], did not considerably vary in the Ti L-edge and O K-edge XAS spectra of the fresh and used B-TiO₂ samples (Fig. S26). Multiple use of B-TiO₂ caused a gradual change in the intensity ratio of the split e_g peaks at ~ 459.3 and 460.3 eV (corresponding to anatase and rutile, respectively) in the Ti L-edge spectra, which implied the progress of phase transformation from anatase to rutile [60]. The diffraction patterns of the fresh and used Ti₄O₇ NTAs showed that the XRD peaks arising from the unique crystalline nature of Ti₄O₇ remained intact (Fig. S27), corroborating the chemical durability. On the other hand, the XRD peaks indicative of anatase phase became more pronounced for B-TiO₂ after use in repeated anodic oxidation, which was likely attributed to Ti^{3+} reoxidation [20].

Marginal change in the diffraction patterns seemed not to properly reflect the steady reduction in the electrical conductivity of Ti₄O₇ with increasing catalytic cycle (though it occurred with Ti₄O₇ than with B-TiO₂ to a much lesser extent), confirmed by the multiple electrochemical measurements (Fig. 5b-c). However, the EPR measurements using fresh and spent Ti₄O₇ samples showed that surface OV states were drastically depleted even after single use in anodic oxidation (Fig. S28). The

possibility that oxygen-deficient sites in Ti₄O₇ would vanish via catalytic application was also supported by a gradual decrease in Ti^{3+} content confirmed by the XPS spectra of pristine and used Ti₄O₇ samples (Fig. S29).

To further examine the practicability of conductive TiO₂-derived anodes, anodic 4-CP oxidation by Ti₄O₇ and B-TiO₂ NTAs was performed under constant current conditions in continuous operation mode using modular flow reactors (Fig. S30). As illustrated in Fig. S31, top and bottom cover plates physically clamped the reactor with internal volume of 50 mL that was sandwiched between the anode/cathode pair. Inlet and outlet ports were placed on the opposite sides of the reactor, and feed was supplied using a Masterflex L/S peristaltic pump (set at 10 revolutions per minute (rpm)) at flow rate of 10 mL/min in parallel to the electrodes. Regardless of anode type, the overall anodic efficiency for 4-CP treatment was improved with respect to module number. Contrasting with the relative performance in batch tests at fixed current density (Fig. 4b), Ti₄O₇ NTA exhibited higher electrocatalytic activity for 4-CP oxidation than B-TiO₂ NTA by a factor of 2–3, which linked up with the lower stability of B-TiO₂ NTA. Long-term electrolysis with B-TiO₂ during the continuous operation of anodic oxidation caused a gradual loss of electrocatalytic activity associated with Ti^{3+} reoxidation and structural damage as confirmed by the post-mortem analysis (inset of Figs. 1c and S25 and S27).

4. Conclusions

In this study, comparative assessment of two conductive titanium oxides, prepared via hydrogen annealing and cathodic polarization to induce oxygen non-stoichiometry, was performed in terms of electrical properties, anodic performance and degradative pathways, and prolonged stability. Aligned with the higher electrocatalytic activity of Ti₄O₇ than that of B-TiO₂ confirmed by Nyquist and Mott-Schottky plots, I-V characteristics, and SECM analysis, Ti₄O₇ NTA exhibited the better performance B-TiO₂ NTA based on the efficiencies for CLER and anodic oxidation of MeOH and 4-CP under varying voltage conditions. In particular, seven- to eight-fold higher HOCl production of Ti₄O₇ was likely ascribed to its onset potential being nearly 0.16 V lower than that of B-TiO₂. The two TiO₂-derived anodes were not distinguished in terms of major degradative routes based on the effects of alcohol-based radical scavengers, EPR spectral features, treatability of diverse target organics, and product distribution. Performance tests for anodic oxidation run in a repetitive manner and continuous operation mode, measurements of the electrical properties of the fresh and spent samples, and post-mortem analysis collectively suggested the superior long-term stability of Ti₄O₇ over B-TiO₂. Accordingly, future studies to promote the practicability of Magnéli phases need to focus on developing the strategies to further improve the electrocatalytic activity, such as heteroatom doping and co-catalyst deposition. Considering the relatively low stability, self-doping is suited to produce TiO₂-based anodes for select anodic processes operable at low current densities, including disinfection, fouling control, and photoelectrocatalytic oxidation.

CRediT authorship contribution statement

Minjeong Kim: Investigation, Validation, Writing – original draft, Revised manuscript. **Jaemin Choi:** Investigation, Methodology. **Woonghee Lee:** Investigation, Methodology. **Yong-Yoon Ahn:** Methodology. **Hangil Lee:** Investigation, Methodology. **Kangwoo Cho:** Investigation, Validation, Writing – original draft. **Jaesang Lee:** Conceptualization, Formal analysis, Writing – original draft, Revised manuscript.

Declaration of Competing Interest

The authors declare that they have no known competing financial interests or personal relationships that could have appeared to influence

the work reported in this paper.

Data availability

Data will be made available on request.

Acknowledgments

This work was supported by the National Research Foundation of Korea (NRF) Grant funded by the Korean Government (MSTI) (NRF-2022M3H4A4097524).

Appendix A. Supplementary material

Supplementary data associated with this article can be found in the online version at [doi:10.1016/j.apcatb.2023.122993](https://doi.org/10.1016/j.apcatb.2023.122993).

References

- [1] B.P. Chaplin, The prospect of electrochemical technologies advancing worldwide water treatment, *Acc. Chem. Res.* 52 (2019) 596–604, <https://doi.org/10.1021/acs.accounts.8b00611>.
- [2] C.A. Martinez-Huitle, S. Ferro, Electrochemical oxidation of organic pollutants for the wastewater treatment: direct and indirect processes, *Chem. Soc. Rev.* 35 (2006) 1324–1340, <https://doi.org/10.1039/B517632H>.
- [3] J. Radjenovic, D.L. Sedlak, Challenges and opportunities for electrochemical processes as next-generation technologies for the treatment of contaminated water, *Environ. Sci. Technol.* 49 (2015) 11292–11302, <https://doi.org/10.1021/acs.est.5b02414>.
- [4] C. Comninellis, Electrocatalysis in the electrochemical conversion/combustion of organic pollutants for wastewater treatment, *Electrochim. Acta* 39 (1994) 1857–1862, [https://doi.org/10.1016/0013-4686\(94\)85175-1](https://doi.org/10.1016/0013-4686(94)85175-1).
- [5] B. Marselli, J. Garcia-Gomez, P.A. Michaud, M.A. Rodrigo, C. Comninellis, Electrogeneration of hydroxyl radicals on boron-doped diamond electrodes, *J. Electrochem. Soc.* 150 (2003) D79–D83, <https://doi.org/10.1149/1.1553790>.
- [6] J.F. Niu, H. Lin, J.L. Xu, H. Wu, Y.Y. Li, Electrochemical mineralization of perfluorocarboxylic acids (PFCAs) by Ce-doped modified porous nanocrystalline PbO₂ film electrode, *Environ. Sci. Technol.* 46 (2012) 10191–10198, <https://doi.org/10.1021/es302148z>.
- [7] G. Foti, D. Gandini, C. Comninellis, A. Perret, W. Haenni, Oxidation of organics by intermediates of water discharge on IrO₂ and synthetic diamond anodes, *Electrochem. Solid-State Lett.* 2 (1999) 228–230, <https://doi.org/10.1149/1.1390792>.
- [8] Y.U. Shin, H.Y. Yoo, S. Kim, K.M. Chung, Y.G. Park, K.H. Hwang, S.W. Hong, H. Park, K. Cho, J. Lee, Sequential combination of electro-Fenton and electrochemical chlorination processes for the treatment of anaerobically-digested food wastewater, *Environ. Sci. Technol.* 51 (2017) 10700–10710, <https://doi.org/10.1021/acs.est.7b02018>.
- [9] Y. Yang, L.C. Kao, Y.Y. Liu, K. Sun, H.T. Yu, J.H. Guo, S.Y.H. Liou, M.R. Hoffmann, Cobalt-doped black TiO₂ nanotube array as a stable anode for oxygen evolution and electrochemical wastewater treatment, *ACS Catal.* 8 (2018) 4278–4287, <https://doi.org/10.1021/acscatal.7b04340>.
- [10] C. Yang, S.S. Shang, X.Y. Li, Oxygen-vacancy-enriched substrate-less SnO_x/La-Sb anode for high-performance electrocatalytic oxidation of antibiotics in wastewater, *J. Hazard. Mater.* 436 (2022) 129212, <https://doi.org/10.1016/j.jhazmat.2022.129212>.
- [11] S.O. Ganiyu, N. Oturan, S. Raffy, M. Cretin, R. Esmilaire, E. van Hullebusch, G. Esposito, M.A. Oturan, Sub-stoichiometric titanium oxide (Ti₄O₇) as a suitable ceramic anode for electrooxidation of organic pollutants: a case study of kinetics, mineralization and toxicity assessment of amoxicillin, *Water Res.* 106 (2016) 171–182, <https://doi.org/10.1016/j.watres.2016.09.056>.
- [12] J.B. Wang, D. Zhi, H. Zhou, X.W. He, D.Y. Zhang, Evaluating tetracycline degradation pathway and intermediate toxicity during the electrochemical oxidation over a Ti/Ti₄O₇ anode, *Water Res.* 137 (2018) 324–334, <https://doi.org/10.1016/j.watres.2018.03.030>.
- [13] K.X. Wang, K. Zhao, X. Qin, S. Chen, H.T. Yu, X. Quan, Treatment of organic wastewater by a synergic electrocatalysis process with Ti³⁺ self-doped TiO₂ nanotube arrays electrode as both cathode and anode, *J. Hazard. Mater.* 424 (2022), 127747, <https://doi.org/10.1016/j.jhazmat.2021.127747>.
- [14] D. Zu, H.Y. Wang, S. Lin, G. Ou, H.H. Wei, S.Q. Sun, H. Wu, Oxygen-deficient metal oxides: synthesis routes and applications in energy and environment, *Nano Res.* 12 (2019) 2150–2163, <https://doi.org/10.1007/s12274-019-2377-9>.
- [15] D.B. Migas, V.L. Shaposhnikov, V.E. Borisenko, Tungsten oxides. II. The metallic nature of Magneli phases, *J. Appl. Phys.* 108 (2010) 093714, <https://doi.org/10.1063/1.3505689>.
- [16] F.C. Walsh, R.G.A. Wills, The continuing development of Magneli phase titanium sub-oxides and Ebonex electrodes, *Electrochim. Acta* 55 (2010) 6342–6351, <https://doi.org/10.1016/j.electacta.2010.05.011>.
- [17] C.Q. Huang, Q.C. Zhu, W. Zhang, P.C. Qi, Q. Xiao, Y. Yu, Facile preparation of W₅O₁₄ nanosheet arrays with large crystal channels as high-performance negative electrode for supercapacitor, *Electrochim. Acta* 330 (2020), 135209, <https://doi.org/10.1016/j.electacta.2019.135209>.
- [18] A. Minguzzi, C.M. Sanchez-Sanchez, A. Gallo, V. Montiel, S. Rondinini, Evidence of facilitated electron transfer on hydrogenated self-doped TiO₂ nanocrystals, *ChemElectroChem* 1 (2014) 1415–1421, <https://doi.org/10.1002/celec.201300226>.
- [19] C.Y. Mao, F. Zuo, Y. Hou, X.H. Bu, P.Y. Feng, In situ preparation of a Ti³⁺ self-doped TiO₂ film with enhanced activity as photoanode by N₂H₄ reduction, *Angew. Chem. Int. Ed.* 53 (2014) 10485–10489, <https://doi.org/10.1002/anie.201406017>.
- [20] J.J. Cai, M.H. Zhou, Y.W. Pan, X.D. Du, X.Y. Lu, Extremely efficient electrochemical degradation of organic pollutants with co-generation of hydroxyl and sulfate radicals on Blue-TiO₂ nanotubes anode, *Appl. Catal. B Environ.* 257 (2019), 117902, <https://doi.org/10.1016/j.apcatb.2019.117902>.
- [21] C.L. Meng, Q.F. Zhuo, A.Q. Wang, J.J. Liu, Z.H. Yang, J.F. Niu, Efficient electrochemical oxidation of COVID-19 treatment drugs favipiravir by a novel flow-through Ti/TiO₂-NTA/Ti₄O₇ anode, *Electrochim. Acta* 430 (2022), 141055, <https://doi.org/10.1016/j.electacta.2022.141055>.
- [22] K. Cho, S. Lee, H. Kim, H.E. Kim, A. Son, E.J. Kim, M.K. Li, Z.M. Qiang, S.W. Hong, Effects of reactive oxidants generation and capacitance on photoelectrochemical water disinfection with self-doped titanium dioxide nanotube arrays, *Appl. Catal. B Environ.* 257 (2019), 117910, <https://doi.org/10.1016/j.apcatb.2019.117910>.
- [23] P. Geng, J.Y. Su, C. Miles, C. Comninellis, G.H. Chen, Highly-ordered Magneli Ti₄O₇ nanotube arrays as effective anodic material for electro-oxidation, *Electrochim. Acta* 153 (2015) 316–324, <https://doi.org/10.1016/j.electacta.2014.11.178>.
- [24] H.J. Chen, J. Liang, L. Li, B.Z. Zheng, Z.S. Feng, Z.Q. Xu, Y.L. Luo, Q. Liu, X.F. Shi, Y. Liu, S.Y. Gao, A.M. Asiri, Y. Wang, Q.Q. Kong, X.P. Sun, Ti₂O₃ nanoparticles with Ti³⁺ sites toward efficient NH₃ electro-synthesis under ambient conditions, *ACS Appl. Mater. Interfaces* 13 (2021) 41715–41722, <https://doi.org/10.1021/acsami.1c11872>.
- [25] H.J. Chen, Z.Q. Xu, S.J. Sun, Y.S. Luo, Q. Liu, M.S. Hamdy, Z.S. Feng, X.P. Sun, Y. Wang, Plasma-etched Ti₂O₃ with oxygen vacancies for enhanced NH₃ electrosynthesis and Zn-N₂ batteries, *Inorg. Chem. Front.* 9 (2022) 4608–4613, <https://doi.org/10.1039/D2QI01173E>.
- [26] H. Norenberg, G.A.D. Briggs, Surface structure of the most oxygen deficient Magneli phase - an STM study of Ti₄O₇, *Surf. Sci.* 402 (1998) 738–741, [https://doi.org/10.1016/S0039-6028\(97\)01000-5](https://doi.org/10.1016/S0039-6028(97)01000-5).
- [27] S.O. Ganiyu, N. Oturan, S. Raffy, M. Cretin, C. Causserand, M.A. Oturan, Efficiency of plasma elaborated sub-stoichiometric titanium oxide (Ti₄O₇) ceramic electrode for advanced electrochemical degradation of paracetamol: in different electrolyte media, *Sep. Purif. Technol.* 208 (2019) 142–152, <https://doi.org/10.1016/j.seppur.2018.03.076>.
- [28] S.T. Liang, H. Lin, X.F. Yan, Q.G. Huang, Electro-oxidation of tetracycline by a Magneli phase Ti₄O₇ porous anode: Kinetics, products, and toxicity, *Chem. Eng. J.* 332 (2018) 628–636, <https://doi.org/10.1016/j.cej.2017.09.109>.
- [29] C. Kim, S. Kim, J. Choi, J. Lee, J.S. Kang, Y.E. Sung, J. Lee, W. Choi, J. Yoon, Blue TiO₂ nanotube array as an oxidant generating novel anode material fabricated by simple cathodic polarization, *Electrochim. Acta* 141 (2014) 113–119, <https://doi.org/10.1016/j.electacta.2014.07.062>.
- [30] J. Kim, C. Lee, J. Yoon, Electrochemical peroxodisulfate (PDS) generation on a self-doped TiO₂ nanotube array electrode, *Ind. Eng. Chem. Res.* 57 (2018) 11465–11471, <https://doi.org/10.1021/acs.iecr.8b01208>.
- [31] C. Wang, T.N. Zhang, L.F. Yin, C.S. Ni, J.P. Ni, L.A. Hou, Enhanced perfluorooctane acid mineralization by electrochemical oxidation using Ti³⁺ self-doping TiO₂ nanotube arrays anode, *Chemosphere* 286 (2022), 131804, <https://doi.org/10.1016/j.chemosphere.2021.131804>.
- [32] Y. Zhou, C.H. Chen, N.N. Wang, Y.Y. Li, H.M. Ding, Stable Ti³⁺ self-doped anatase-rutile mixed TiO₂ with enhanced visible light utilization and durability, *J. Phys. Chem. C* 120 (2016) 6116–6124, <https://doi.org/10.1021/acs.jpcc.6b00655>.
- [33] H.H. Pan, M.H. Sun, X.G. Wang, M. Zhang, M. Murugananthan, Y.R. Zhang, A novel electric-assisted photocatalytic technique using self-doped TiO₂ nanotube films, *Appl. Catal. B Environ.* 307 (2022), 121174, <https://doi.org/10.1016/j.apcatb.2022.121174>.
- [34] J.Y. Kim, K.J. Lee, S.H. Kang, J. Shin, Y.E. Sung, Enhanced photovoltaic properties of a cobalt bipyridyl redox electrolyte in dye-sensitized solar cells employing vertically aligned TiO₂ nanotube electrodes, *J. Phys. Chem. C* 115 (2011) 19979–19985, <https://doi.org/10.1021/jp2025736>.
- [35] M. Paulose, K. Shankar, S. Yoriya, H.E. Prakasham, O.K. Varghese, G.K. Mor, T. J. LaTempa, A. Fitzgerald, C.A. Grimes, Anodic growth of highly ordered TiO₂ nanotube arrays to 134 μm in length, *J. Phys. Chem. B* 110 (2006) 16179–16184, <https://doi.org/10.1021/jp064020k>.
- [36] S. Lee, G.H. Lee, J.C. Kim, D.W. Kim, Magneli-phase Ti₄O₇ nanosphere electrocatalyst support for carbon-free oxygen electrodes in lithium-oxygen batteries, *ACS Catal.* 8 (2018) 2601–2610, <https://doi.org/10.1021/acscatal.7b03741>.
- [37] C. Kim, S. Kim, J. Choi, J. Lee, J.S. Kang, Y.-E. Sung, J. Lee, W. Choi, J. Yoon, Blue TiO₂ nanotube array as an oxidant generating novel anode material fabricated by simple cathodic polarization, *Electrochim. Acta* 141 (2014) 113–119.
- [38] W. Lee, T. Lee, S. Kim, S. Bae, J. Yoon, K. Cho, Descriptive role of Pt/PtOx ratio on the selective chlorine evolution reaction under polarity reversal as studied by scanning electrochemical microscopy, *ACS Appl. Mater. Interfaces* 13 (2021) 34093–34101, <https://doi.org/10.1021/acsami.1c06187>.
- [39] L. Moberg, B. Karlberg, An improved N, N'-diethyl-p-phenylenediamine (DPD) method for the determination of free chlorine based on multiple wavelength detection, *Anal. Chim. Acta* 407 (2000) 127–133.

- [40] C. Liang, C.-F. Huang, N. Mohanty, R.M. Kurakalva, A rapid spectrophotometric determination of persulfate anion in ISCO, *Chemosphere* 73 (2008) 1540–1543.
- [41] A. Kumar, N.H. Barbhuiya, S.P. Singh, Magneli phase titanium sub-oxides synthesis, fabrication and its application for environmental remediation: current status and prospect, *Chemosphere* 307 (2022), 135878, <https://doi.org/10.1016/j.chemosphere.2022.135878>.
- [42] L. Hao, H.W. Huang, Y.H. Zhang, T.Y. Ma, Oxygen vacant semiconductor photocatalysts, *Adv. Funct. Mater.* 31 (2021) 2100919, <https://doi.org/10.1002/adfm.202100919>.
- [43] H. Zhou, Y.R. Zhang, Electrochemically self-doped TiO₂ nanotube arrays for supercapacitors, *J. Phys. Chem. C* 118 (2014) 5626–5636, <https://doi.org/10.1021/jp4082883>.
- [44] J. Lim, Y. Yang, M.R. Hoffmann, Activation of peroxydisulfate by oxygen vacancies-enriched cobalt-doped black TiO₂ nanotubes for the removal of organic pollutants, *Environ. Sci. Technol.* 53 (2019) 6972–6980, <https://doi.org/10.1021/acs.est.9b01449>.
- [45] M. Ishfaq, M.R. Khan, M.F. Bhopal, F. Nasim, A. Ali, A.S. Bhatti, I. Ahmed, S. Bhardwaj, C. Cepek, 1.5 MeV proton irradiation effects on electrical and structural properties of TiO₂/n-Si interface, *J. Appl. Phys.* 115 (2014), 174506, <https://doi.org/10.1063/1.4874942>.
- [46] Y.F. Xu, S.J. Wu, P.P. Wan, J.G. Sun, Z.D. Hood, Introducing Ti³⁺ defects based on lattice distortion for enhanced visible light photoreactivity in TiO₂ microspheres, *RSC Adv.* 7 (2017) 32461–32467, <https://doi.org/10.1039/C7RA04885H>.
- [47] K. Dong, J. Liang, Y.Y. Wang, Y.C. Ren, Z.Q. Xu, H.P. Zhou, L. Li, Q. Liu, Y.L. Luo, T.S. Li, A.M. Asiri, Q. Li, D.W. Ma, X.P. Sun, Plasma-induced defective TiO_{2-x} with oxygen vacancies: a high-active and robust bifunctional catalyst toward H₂O₂ electrosynthesis, *Chem. Catal.* 1 (2021) 1437–1448, <https://doi.org/10.1016/j.che-cat.2021.10.011>.
- [48] J. Lee, Z. Li, L.Z. Zhu, S.H. Xie, X.L. Cui, Ti³⁺ self-doped TiO₂ via facile catalytic reduction over Al(acac)₃ with enhanced photoelectrochemical and photocatalytic activities, *Appl. Catal. B Environ.* 224 (2018) 715–724, <https://doi.org/10.1016/j.apcatb.2017.10.057>.
- [49] X.H. Lu, G.M. Wang, T. Zhai, M.H. Yu, J.Y. Gan, Y.X. Tong, Y. Li, Hydrogenated TiO₂ nanotube arrays for supercapacitors, *Nano Lett.* 12 (2012) 1690–1696, <https://doi.org/10.1021/nl300173j>.
- [50] T. Lee, W. Lee, S. Kim, C. Lee, K. Cho, C. Kim, J. Yoon, High chlorine evolution performance of electrochemically reduced TiO₂ nanotube array coated with a thin RuO₂ layer by the self-synthetic method, *RSC Adv.* 11 (2021) 12107–12116, <https://doi.org/10.1039/D0RA09623G>.
- [51] A. Monod, A. Chebbi, R. Durand-Jolibois, P. Carlier, Oxidation of methanol by hydroxyl radicals in aqueous solution under simulated cloud droplet conditions, *Atmos. Environ.* 34 (2000) 5283–5294, [https://doi.org/10.1016/S1352-2310\(00\)00191-6](https://doi.org/10.1016/S1352-2310(00)00191-6).
- [52] Y.U. Shin, H.Y. Yoo, Y.Y. Ahn, M.S. Kim, K. Lee, S. Yu, C. Lee, K. Cho, H.I. Kim, J. Lee, Electrochemical oxidation of organics in sulfate solutions on boron-doped diamond electrode: Multiple pathways for sulfate radical generation, *Appl. Catal. B Environ.* 254 (2019) 156–165, <https://doi.org/10.1016/j.apcatb.2019.04.060>.
- [53] J.L. Cao, H.Y. Zhao, F.H. Cao, J.Q. Zhang, C.N. Cao, Electrocatalytic degradation of 4-chlorophenol on F-doped PbO₂ anodes, *Electrochim. Acta* 54 (2009) 2595–2602, <https://doi.org/10.1016/j.electacta.2008.10.049>.
- [54] P. Neta, V. Madhavan, H. Zemel, R.W. Fessenden, Rate constants and mechanism of reaction of SO₄^{•−} with aromatic compounds, *J. Am. Chem. Soc.* 99 (1977) 163–164, <https://doi.org/10.1021/ja00443a030>.
- [55] H.Y. Cai, J. Zou, J.N. Lin, J.W. Li, Y.X. Huang, S.Y. Zhang, B.L. Yuan, J. Ma, Sodium hydroxide-enhanced acetaminophen elimination in heat/peroxydisulfate system: production of singlet oxygen and hydroxyl radical, *Chem. Eng. J.* 429 (2022), 132438, <https://doi.org/10.1016/j.cej.2021.132438>.
- [56] E. Moctezuma, E. Leyva, C.A. Aguilar, R.A. Luna, C. Montalvo, Photocatalytic degradation of paracetamol: intermediates and total reaction mechanism, *J. Hazard. Mater.* 243 (2012) 130–138, <https://doi.org/10.1016/j.jhazmat.2012.10.010>.
- [57] J.L. Amplett, G. Denuault, Scanning electrochemical microscopy (SECM): an investigation of the effects of tip geometry on amperometric tip response, *J. Phys. Chem. B* 102 (1998) 9946–9951, <https://doi.org/10.1021/jp982829u>.
- [58] E.T. Yun, W. Lee, Y.Y. Ahn, J. Choi, J.D. Fortner, K. Cho, S. Hong, J. Lee, Dual role of N-doped graphene film as a cathode material for anodic organic oxidation and persulfate production and as a planar carbocatalyst for non-electrochemical persulfate activation, *Environ. Sci. Nano* 9 (2022) 1662–1674, <https://doi.org/10.1039/D1EN01188J>.
- [59] V.R. Mastelaro, P.P. Neves, S.R. de Lazaro, E. Longo, A. Michalowicz, J.A. Eiras, Electronic structure of Pb_{1-x}La_xTiO₃ ferroelectric materials from Ti 2p and O 1s soft X-ray absorption spectroscopy, *J. Appl. Phys.* 99 (2006), 044104, <https://doi.org/10.1063/1.2173683>.
- [60] A. Gloter, C. Ewels, P. Umek, D. Arcon, C. Colliex, Electronic structure of titania-based nanotubes investigated by EELS spectroscopy, *Phys. Rev. B* 80 (2009), 035413, <https://doi.org/10.1103/PhysRevB.80.035413>.